

Structure of Corrosion Layers on Archaeological Iron Artifacts From Nanhai I

Minghao Jia

Peking University School of Archaeology and Museology

Pei Hu

Peking University School of Archaeology and Museology

Zisang Gong

Peking University School of Archaeology and Museology

Yadong Xue

Peking University School of Archaeology and Museology

Yufan Hou

Peking University School of Archaeology and Museology

Jian Sun

National Centre for Archaeology

Yong Cui

Guangdong Provincial Institute of Cultural Relics and Archaeology

Dongbo Hu

Peking University School of Archaeology and Museology

Gang Hu (✉ hug71@163.com)

Peking University School of Archaeology and Museology

Research Article

Keywords: Nanhai I, Archaeological iron, Corrosion layers, Preservation

Posted Date: May 5th, 2021

DOI: <https://doi.org/10.21203/rs.3.rs-479807/v1>

License:  This work is licensed under a Creative Commons Attribution 4.0 International License.

[Read Full License](#)

Structure of corrosion layers on archaeological iron artifacts from Nanhai I

Minghao Jia¹, Pei Hu¹, Zisang Gong¹, Yadong Xue¹, Yufan Hou¹,
Jian Sun², Yong Cui³, Dongbo Hu¹, Gang Hu^{1,*}

*Correspondence: hugang@pku.edu.cn

School of Archaeology and Museology, Peking University 100871, Beijing, China

Full list of author information is available at the end of the article.

Abstract

Thousands of archaeological irons were excavated from the Nanhai I ship of the Southern Song Dynasty sunk in South China Sea, most of which were severely corroded and fragmented. To understand the current corrosion state and guide the restoration and protection, one piece of these iron objects was selected for analysis. Using optical microscope, scanning electron microscope, micro-laser Raman spectroscopy, infrared spectroscopy, and X-ray diffraction, it was clear that the archaeological iron was hypereutectic white iron with carbon content of about 4.3-6.69% and had experienced low melt undercooling. There were many internal cracks formed by general corrosion extending to the iron core which was a tendency of instability. At the interface between the iron and rust, there was a black dense layer enriched with chlorine and a loose outer layer in yellow. The dense layer was mainly composed of magnetite, akaganeite and maghemite, while the rust of the loose layer was about lepidocrocite, goethite, ferroxhite, maghemite and hematite. Besides, the major phases of all corrosion products were akaganeite and lepidocrocite. Numerous holes and cracks in the rust layer had no barrier ability to the outside electrolyte, so that the iron core formed many redox electrochemical sites to be general corrosion with the rust. Meanwhile, the dense rust close to the iron core was broken locally by enriched chlorine layer, which was extremely detrimental to the stability of the archaeological iron. By electrochemical impedance spectroscopy, it could be determined that the rust layers had no protective effect on the internal iron core indeed under the condition of simulating seawater, even accelerating corrosion. The mechanism of the rust growth was proposed from the shipwreck sinking to the laboratory testing to explain the entire corrosion process. Based on the concept of authenticity on the preservation, the archaeological rusted iron of the Nanhai I ship excavated from marine environment should be properly dechlorinated and necessarily stabilized, such as corrosion inhibition and reinforcement, for the rust structure and the internal iron core well-retained together.

Keywords: Nanhai I, Archaeological iron, Corrosion layers, Preservation

Introduction

Nanhai I is a wooden merchant ship of the Southern Song Dynasty (1,127-1,279 A.D.) that was excavated in Guangdong Province and is now displayed in the Maritime Silk Road Museum of Guangdong [1]. Judging from the hull structure, it could be called as “Fu Ship (Fujian-style Freighter)” which belonged to a typical type in ancient China. It is the oldest, largest, and best-preserved one among the sunken ships found so far for international trade. The wreck may be defined in the era of the mid-13th century due to the overloaded goods on board [2]. It provides numerous historical information about the Maritime Silk Road and extremely rare materials for the study of ancient overseas trade.

In ancient trade, metal raw materials and products dominate the international market, and can be used to make weapons and labor tools [3]. A huge number of daily necessities and commercial products which made of iron or steel, such as pots, nails, and long slabs, were excavated from the Nanhai I. How to stabilize them under favorable conditions against further corrosion has been a serious problem. Further corrosion of the iron objects often occurs after extraction from marine condition and exposing to a new environment that tended to transform the metal core into corrosion products. Several articles have focused on the structure and composition of the rust layers of iron or steel [4-6]. They believed that the distribution of different components in the rust layer had remarkable effects on the future corrosion. In marine, the long-term immersion of iron is prone to form thick rust with many different phases: oxides, oxyhydroxides, sulphides, sulphates, chlorides, etc. Besides, the prior phases of rusts are usually a complex mixed with goethite (α -FeOOH), akaganeite (β -FeOOH), lepidocrocite (γ -FeOOH), and magnetite (Fe_3O_4) [7]. The rust composition and distribution of archaeological irons are always more complicated than the simulated in the laboratory, especially under natural marine corrosion for more than 800 years. Determining the state of rust are beneficial to infer its corrosion mechanism and predict future corrosion for the conservationists.

This article reported the metallic phase of iron materials in the Southern Song Dynasty of China and analyzed the rust state of marine corrosion over hundreds of years to provide useful information for preventing further degradation of iron artifacts after salvation and ensuring its preservation. The iron fragments covered with rust from the Nanhai I ship were this research objects. The rust was mainly analyzed by optical stereomicroscopy, micro-Raman spectroscopy and electrochemical impedance spectroscopy combined with SEM, XRD, and FTIR to evaluate the current corrosion and try to find the corrosion causes during marine period and after salvation.

Materials and Methods

Archaeological iron objects

The iron samples were all collected from the Nanhai I ship. The initial states of these archaeological iron were multiple stacked and completely covered by rust and mud. They were placed in a pH=9 sodium hydroxide solution during transportation to archaeological laboratory. Most of them have been completely corroded and shattered. During initial cleaning with deionized water to remove the silt and mud, the rust layers were gradually exposed. The surface appearance and the approximate dimensions shown in Fig.1.



Fig. 1 Archaeological iron artifacts coming from Nanhai I (Guangdong, China) with rust

Samples Preparation

Rust powder: The rust powder was scraped from the iron object with a razor and a brush, and then the rust was milled in an agate mortar for a uniform and fine size.

Cross-section of iron core and rust layers: The sample was cut from the edge of the archaeological iron and then dried with a dryer at room temperature to remove free water on the surface. The object was embedded in epoxy resin, and then mechanically grinding using SiC paper (grade 80–2000) under absolute ethanol. Finally, this sample was polished with diamond paste to obtain a smooth cross-section.

Working electrode: Cutting along the above cutting edge to ensure the continuity and similarity of the rust layers and the iron core. The sample was cut in a small piece of 10 mm × 10 mm. It was carefully embedded in epoxy resin to mask and protect the cut edges for electrochemical impedance test. The details were shown in Fig. 2.

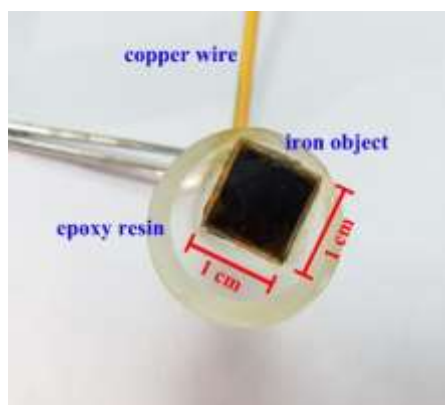


Fig. 2 Working electrode for electrochemical impedance test

Morphology observation

Optical stereomicroscope (Nikon Eclipse LV100ND, Japan) with digital camera (Nikon DS-Ri2, Japan) was used to observe the metallographic structure of the iron core and the appearance of the rust layers of the cross-section.

Scanning electron microscope (FEI Quanta 200F, Netherlands) was used to show the morphology of the sample surface in detail under an accelerating voltage of 10 kV.

Determination of rust composition

To determine the crystalline structure of the rust powder, X-ray diffraction patterns were recorded by a diffractometer (PANanalytical X'pert-3 Power, Netherlands) with Cu anode. The generator voltage was 40 kV and tube current was 40 mA. Angular scanning was performed from 5° to 80° with a scan step size of 0.013° . The rust was previously powdered and screened to a particle size of less than $125\ \mu\text{m}$.

KBr-matrix pellets were prepared to define chemical structures of rust using FTIR transmittance analysis (Bruker Tensor 27, Germany) in the ranges from 400 to $4000\ \text{cm}^{-1}$ at $4\ \text{cm}^{-1}$ resolution. $0.2\ \text{mg}$ of powder sample was mixed with $200\ \text{mg}$ of dry KBr ($> 99\%$ FTIR grade, Sigma-Aldrich), then milled in an agate mortar and pressed to be pellets.

Different rust components were defined by micro-Raman spectroscopy performed on the cross-section sample using micro-Raman spectroscope (Thermo Scientific DXRxi, America) with a microscope (OLYMPUS BX51, Japan). Raman excitation was provided by a frequency doubled Nd:YAG laser operating at $532\ \text{nm}$ with a power of about $0.2\ \text{mW}$ and with a probe diameter of about $1\ \text{mm}$. All spectra were calibrated using the $519.5\ \text{cm}^{-1}$ line of a silicon wafer.

Electrochemical impedance

Electrochemical impedance spectroscopy of rusted and naked archaeological iron objects were investigated using an electrochemical workstation (CorrTestTM CS-350, China). Measurements were carried out in a three-electrode cell with $1.5\ \text{g/L}$ NaCl and $1.5\ \text{g/L}$ Na₂SO₄ mixture as an electrolyte to simulate sea water. The three-electrode cell includes a saturated calomel reference electrode filled with saturated KCl solution which served as a reference electrode, a platinum auxiliary electrode with an exposure surface of $10\ \text{mm} \times 10\ \text{mm}$ as a counter electrode, and the iron objects with an exposure surface of $1\ \text{cm}^2$ as working electrode as described above. Prior to impedance tests, the

electrodes were kept in the solution for 30 min to stabilize the free corrosion potential. Tests were performed at open circuit potential in an applied frequency ranged from 100 kHz to 10 mHz, and the sinusoidal perturbation signal with 10 mV amplitude was used. The obtained data were interpreted based on equivalent circuit using Zview to obtain the fitting parameters.

Results and Discussion

Cracks in the archaeological iron

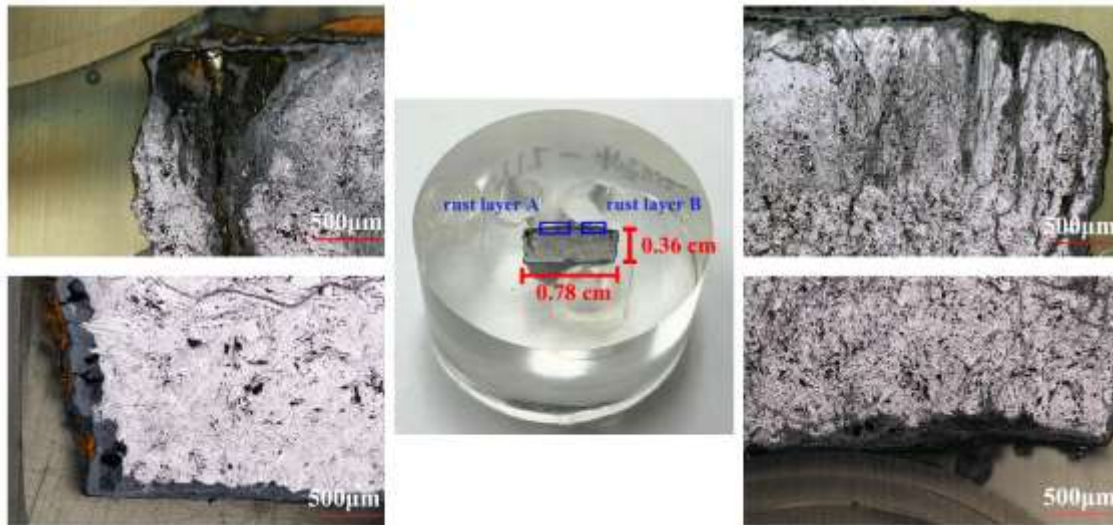


Fig. 3 Digital and microscopic graphs of the cross-section of archaeological iron

After grinding and polishing, the cross-section sample has shown a significant corrosion state without any corrosive agent. The cross-section had a length of 0.78 cm and a width of 0.36 cm, which was approximately a rectangular plane. General corrosion and long cracks extending from the rust layer to the iron core were clearly observed, and the state of the upper surface was the most obvious. There was a worryingly large crack in the upper left corner, which should be caused by the combined effect of general corrosion and crevice corrosion. Due to the internal stress of corrosion products [8], it would gradually expand the core and tend to peel off a small part from the metal object. The cracks in the upper right corner were densely distributed and intersected, extending in different directions to the core, which was not conducive to a stable storage of the archaeological iron. Then, this embedded sample will continue to be used to analyze the cast state of the iron core and the composition of the rust layer on the upper surface.

Metallographic of the archaeological iron

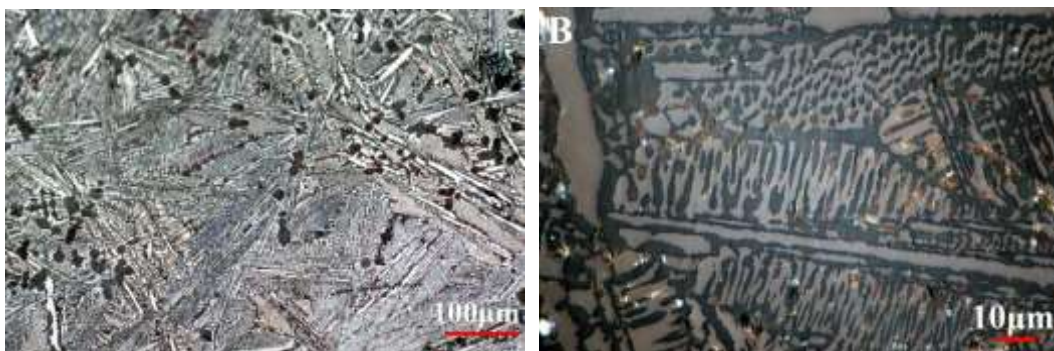


Fig. 4 Metallographic diagrams of archaeological iron artifact from Nanhai I

The cross-section was silvery white. The white and long strips were primary cementite, and

the matrix was eutectic ledeburite. The archaeological sample was a typical hypereutectic white cast iron with high carbon content in the range of 4.3%-6.69 wt.%.

When the hypereutectic molten iron was cooled, the wide and coarse primary cementite was produced first. Just because it could grow freely in the liquid, it was shaped as strips or flakes. Then, the temperature of the metal liquid continued to drop, and the eutectic phase occurred to be eutectic ledeburite. Due to the local cooling, primary cementite and eutectic ledeburite were also arranged in different cooling directions [9]. Generally, two major phases of eutectics were normally encountered in white cast irons with high-carbon under different undercoolings. They could be described as ledeburite eutectic which had dendrite branches and another was plate-like eutectic. Besides, plate-like eutectic in white cast irons became the main constituent of the microstructure with increased degree of melt undercooling ($\Delta T \sim 35\text{-}40^\circ\text{C}$), while ledeburite eutectic often appeared at lower undercooling ($\Delta T \sim 5\text{-}25^\circ\text{C}$). This transformation does not really depend on starting alloys composition (hypo- or hyper-eutectic) [9]. The ledeburite in the metallographic images of the archaeological iron section was mostly dendritic. Based on this, it could be inferred that the iron object from the Southern Song Dynasty has experienced slow cooling after casting into a mold.

Composition of the rust powder

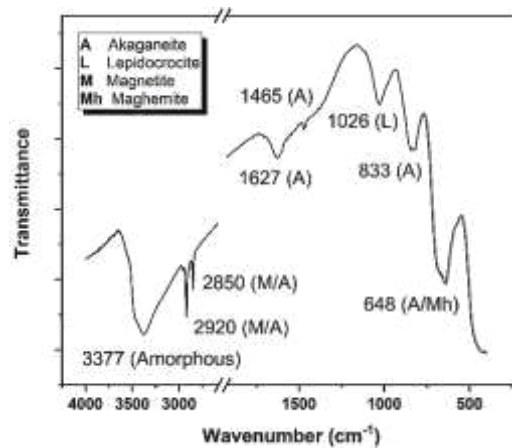


Fig. 5 FT-IR diagram of rust powder

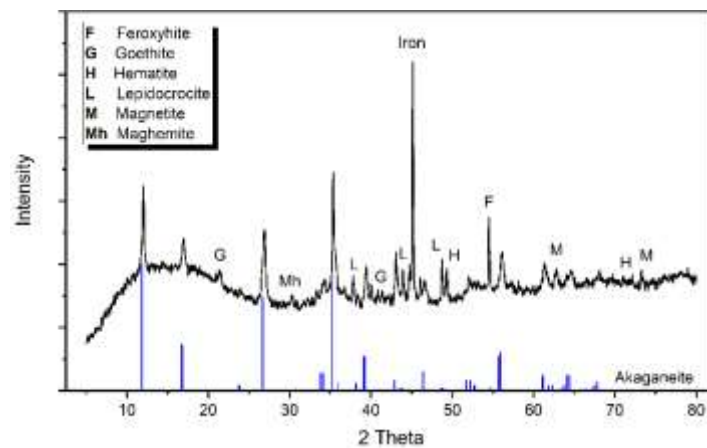


Fig. 6 XRD diagram of rust powder

The basic components of the rust layer were identified by FT-IR. Fig. 5 showed the main component of the powdered rust were mainly akaganeite (β -FeOOH), lepidocrocite (γ -FeOOH), and magnetite (Fe_3O_4) with a small amount of maghemite (γ - Fe_2O_3). The absorption peaks at 833 cm^{-1} and 1627 cm^{-1} were corresponded to the bending of O-H bonds and the vibration of Fe-O bonds in β -FeOOH, respectively [10]. The peak at 1026 cm^{-1} was due to the O-H bending in γ -FeOOH [11]. In addition, the characteristic peak of γ - Fe_2O_3 and β -FeOOH could be overlapped at 648 cm^{-1} , while Fe_3O_4 had two strong characteristic peaks between 2850 - 2950 cm^{-1} , which was also overlapped the position of β -FeOOH [12]. As for the peak of 3377 cm^{-1} , it was a common peak of amorphous rust [10].

Also, XRD was used to analyze the composition of rust powder, combined with data of infrared spectroscopy. XRD spectrum was compared individually by Jade software and PDF-card data. The peaks of the XRD data and the provided standard spectrum of akaganeite could clearly correspond to each other, which could be regarded as the main phase of rust powder. Meanwhile, a significant signal of pure iron appeared, proving that there were some tiny iron particles that peeled off with rust due to corrosion. The peaks intensity of other rust components were weak, but a small amount of goethite (α -FeOOH), lepidocrocite, feroxyhite (δ -FeOOH), hematite (α - Fe_2O_3), maghemite and magnetite could be confirmed according to the PDF information.

Ferric oxyhydroxides has four common types, where goethite was an electrochemically stable phase, whereas others were all active phase and could be transformed into relatively stable magnetite [6]. The results of FT-IR and XRD indicated that a large amount of β -FeOOH was present in the rust, which was associated with the high concentration of chloride in the South China Sea. However, in this work, α -FeOOH was only detected in the XRD with weak intensity and scarce signal in the IR spectra. Most iron-based compounds involved in corrosion reactions were prone to transform into β -FeOOH and γ -FeOOH in marine, resulting in the little amount of α -FeOOH in rust. Generally, there was a fact that the formation of β -FeOOH need chloride ions which could stabilize the structure of its crystal [13]. Besides, β -FeOOH was the most detrimental to continuous corrosion of archaeological iron among all the ferric oxyhydroxides [14]. Therefore, the composition in the rust powder preliminarily indicated that the rust phase of these archaeological irons had not yet reached stability, and the subsequent stabilization treatment was necessarily required.

Structure of the rust layers

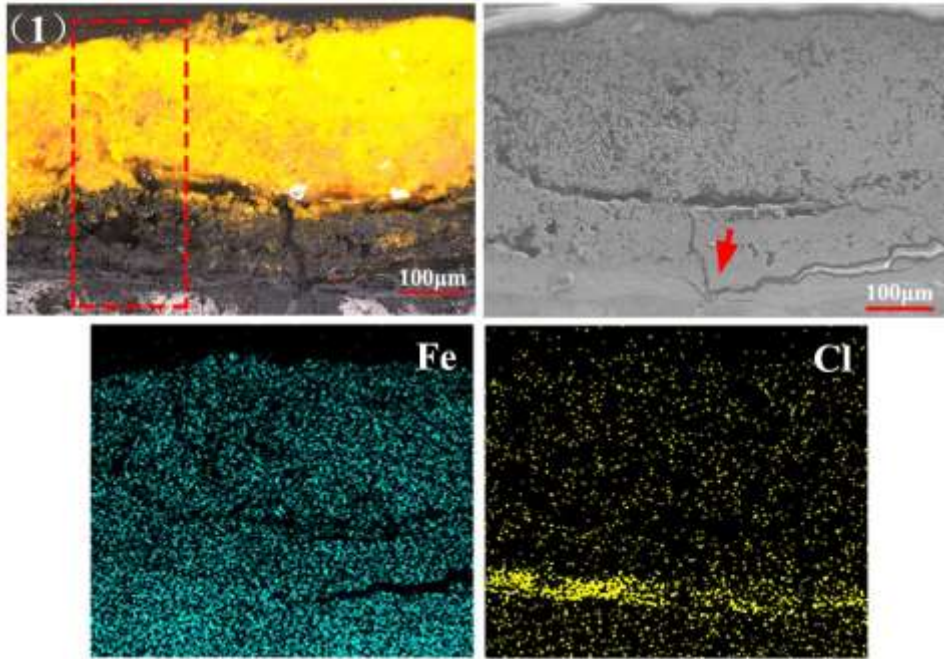


Fig. 7 Graphs of microstructure and element distribution of the rust layer A (red square for Raman analysis)

Fig. 7 showed detail of the rust layer A which marked in fig. 3. The surface of the archaeological iron was mainly divided into two major rust layers: the outer layer was yellow and present a loose and porous appearance, while the inner one close to the iron core was black and dense. Large cracks penetrated the whole rust layer, even breaking into the iron core and cutting the dense black layer to be peeled off easily. The iron element was almost evenly distributed in the whole rust. The chlorine element was evenly distributed in the outer rust and formed a highlight band which coincided with the position of the dense rust layer.

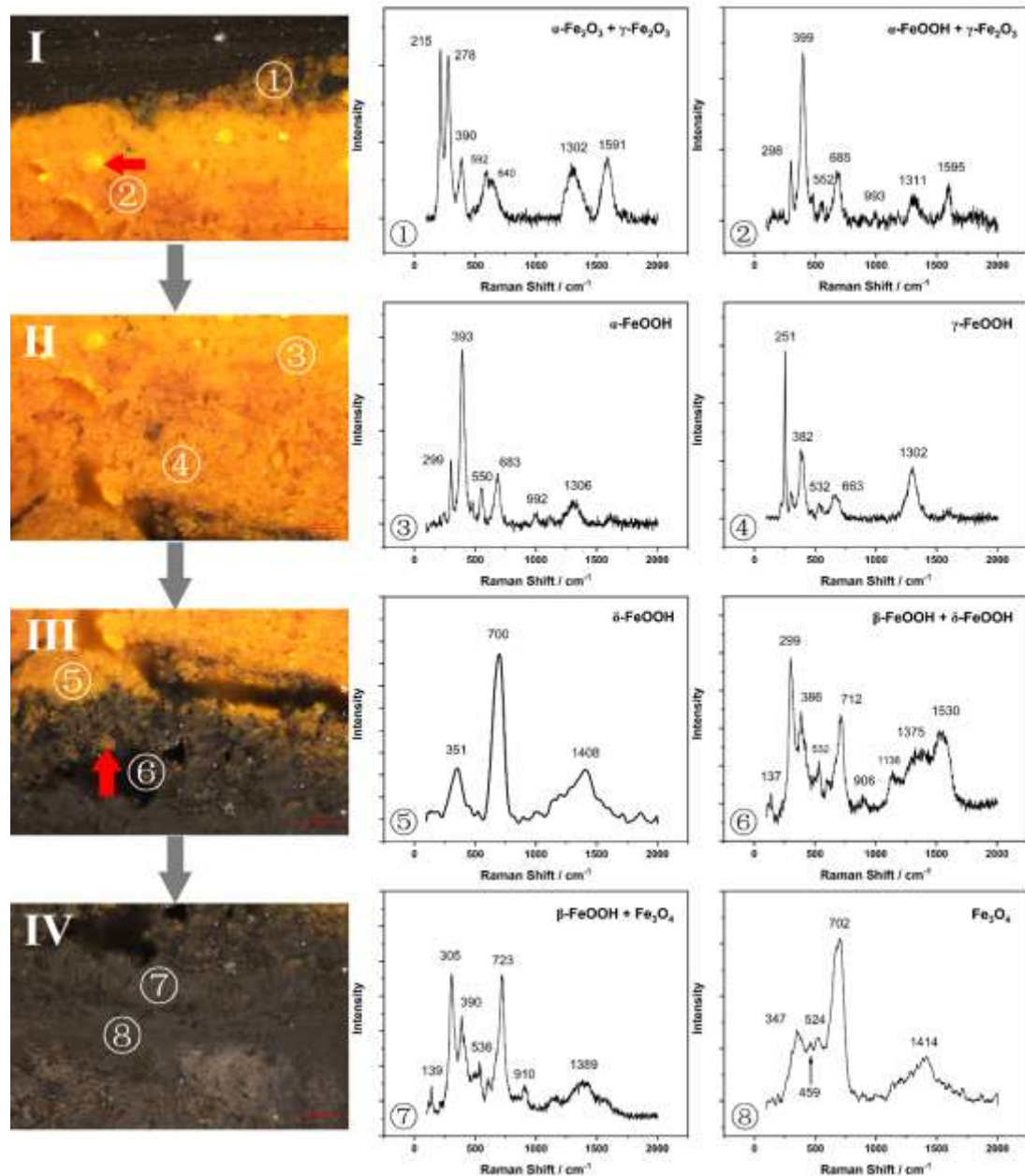


Fig. 8 Raman spectra of the rust layer A (red square in Fig. 7)

Micro-Raman detected eight points respectively in Fig. 8. The oxides and hydroxides of iron compounds were identified layer by layer according to the literature values [7, 15-17]. The cross-section of the rust layer A indicated four distinct layers based on colors: a yellow outermost layer dotted with light-yellow spots (I), a yellow layer (II), a black layer dotted with yellow spots (III), and a black innermost layer which was closely connected with the iron core (IV). Raman spectra showed that the outermost rust was mainly formed by hematite ($\alpha\text{-Fe}_2\text{O}_3$) and maghemite ($\gamma\text{-Fe}_2\text{O}_3$), with characteristic peaks at 215, 278 and 390 cm^{-1} to $\alpha\text{-Fe}_2\text{O}_3$ and the relatively weak peak at 1591 cm^{-1} to $\gamma\text{-Fe}_2\text{O}_3$. The light-yellow dots in the outer rust showed a strong peak at 399 cm^{-1} with less intense peaks at 298, 685 and 1311 cm^{-1} were attributed to the existence of goethite ($\alpha\text{-FeOOH}$). A strongest peak closed to 251 cm^{-1} and a second peak in the Raman shift of 382 cm^{-1} was related to

the lepidocrocite phase (γ -FeOOH) which coexisted in the middle part of the yellow rust layer with α -FeOOH phase. The presence of feroxyhite (δ -FeOOH) was confirmed by its characteristic bands at 351 and 700 cm^{-1} at the junction of black and yellow rust. Akaganeite (β -FeOOH) was often regarded as the most dangerous compound in rust due to its hygroscopicity in post-excavation corrosion and easily transformation into other oxides, especially the magnetite (Fe_3O_4) [18]. Besides, chloride ions were often found in the crystal lattice of β -FeOOH, which could lead to complete loss of the artefact [7]. In this object, akaganeite had the bands at 137, 299 and 386 cm^{-1} , while magnetite was assigned the Raman band at 347, 459, 702 and 1414 cm^{-1} . The two kinds of rust had obvious signals near the black dense layer, where chlorine was enriched.

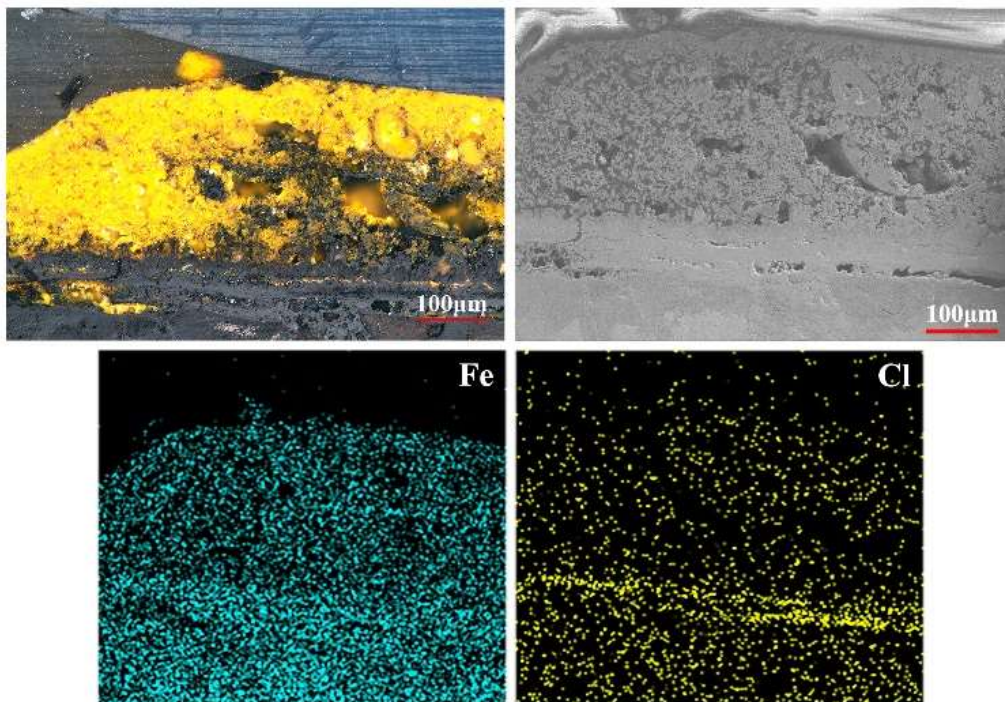


Fig. 9 Graphs of microstructure and element distribution of the rust layer B

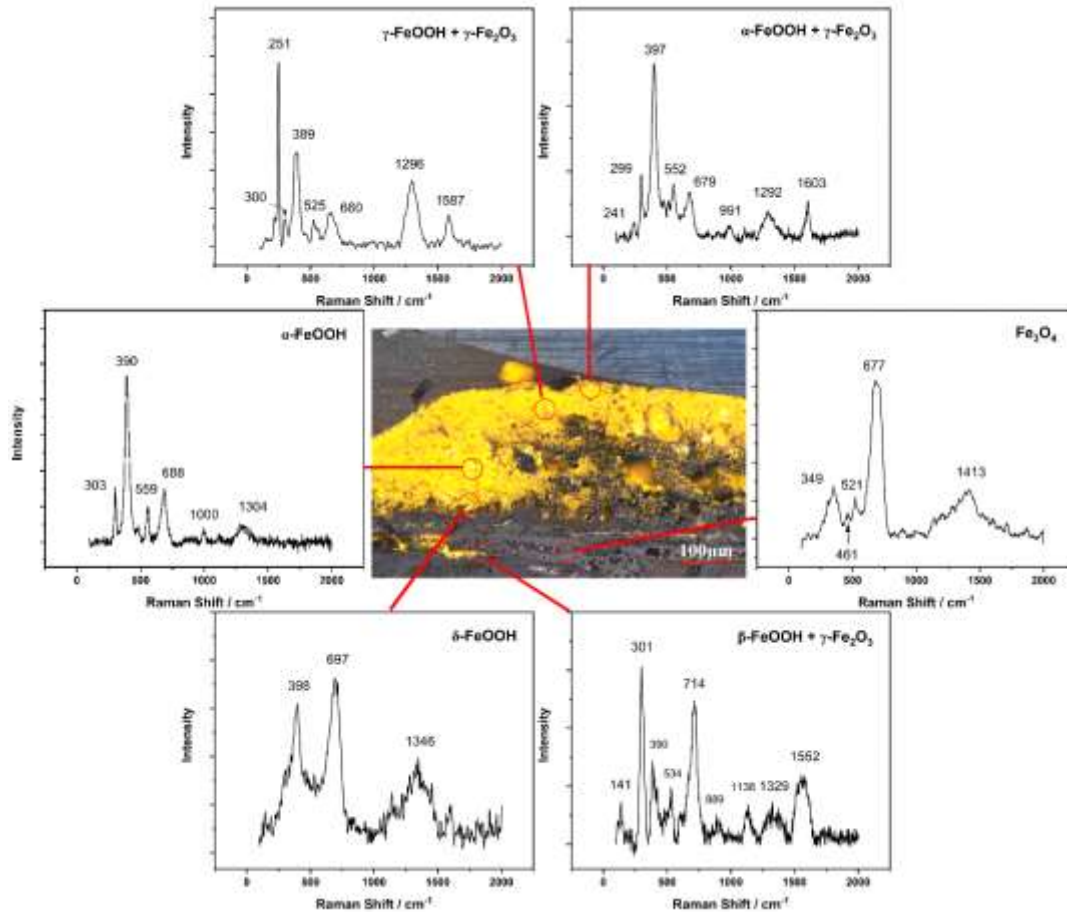


Fig. 10 Raman spectra of the rust layer B

Area B was the rust layer on the upper right of the iron sample. There were several wide and hollow lines at the interface between rust and iron, which did not tightly wrap the internal metal to protect against external environment. The overall structure was similar to that of the layer A, except that the black rust gradually occupied the yellow outer layer. Maghemite, goethite and lepidocrocite were the dominant phases in the yellow loose rust layer, and the black dense layer where chlorine gathered was still mainly composed of akaganeite and magnetite.

Therefore, there were two obvious rust layers on the upper surface of the iron. The loose yellow rust had a tendency of exfoliation and the dense black rust had a lot of cracks, so that the inner iron core still had channels in contact with the external environment which was hard to be stable.

Corrosion evaluation in simulated seawater

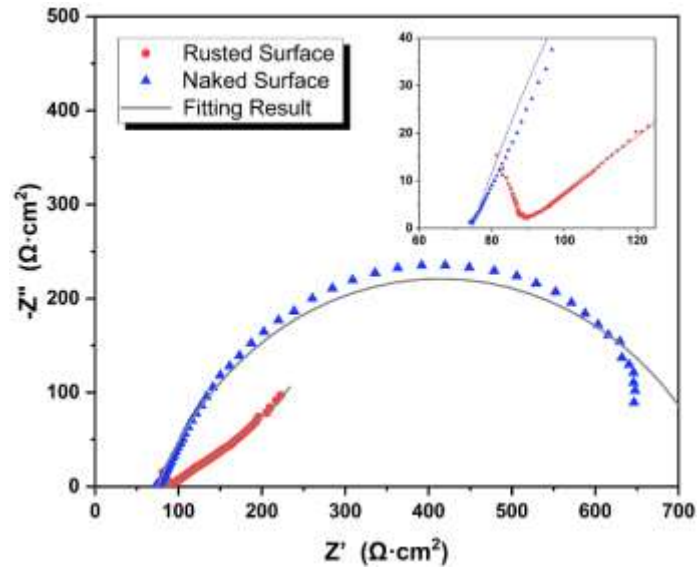


Fig. 11 Nyquist plots of naked and rusted archaeological iron in simulated seawater

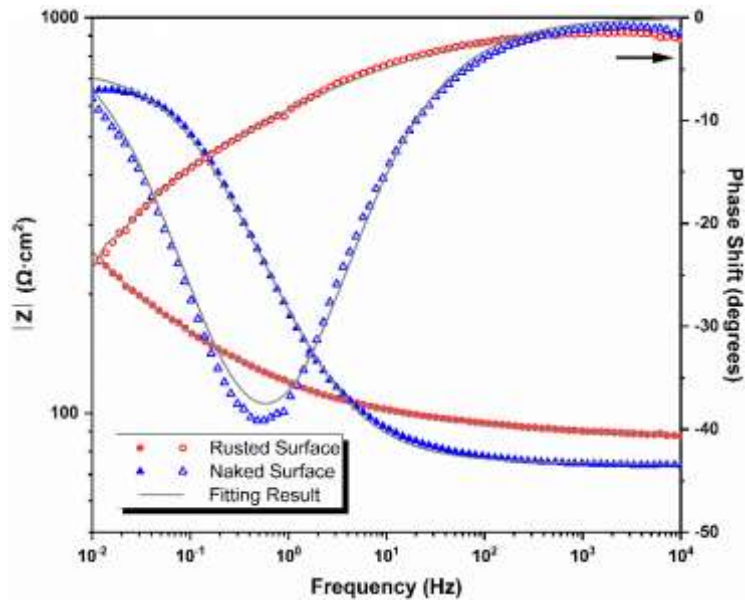


Fig. 12 Bode plots of naked and rusted archaeological iron in simulated seawater

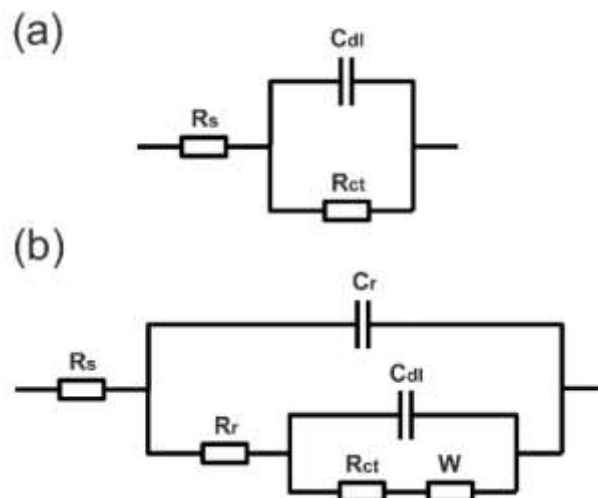


Fig. 13 Equivalent circuit of naked and rusted archaeological iron

Electrochemical impedance spectroscopy (EIS) is an effective tool to get valuable information about the nature of the rust layers formed on the marine-corroded archaeological iron.

Figs. 11 and 12 showed the Nyquist and Bode plots of naked (removing the rust) and rusted archaeological iron, respectively. For the rusted surface, the Nyquist plot was composed of a depressed capacitive semi-arc in the high frequency, and a long tail in the low frequency region representing typical Warburg impedance. The charge transfer resistance of the iron rust dominated at the low frequency region while the rust resistance dominated at the high frequency region [19]. This indicated that the electrochemical corrosion process on the rust/iron interface in NaCl/Na₂SO₄ solution was controlled by the diffusion process. The construction of rust layers could be described using the equivalent circuit in Fig. 13(b). After the rust surface was completely removed, the archaeological sample reacted with the simulated seawater directly. Only one double-layer capacitive semicircle was observed in the Nyquist plot and its equivalent circuit was shown in Fig. 13(a). In Figs. 9(a) and (b), R_S represented the electrolyte resistance, C_r the rust capacitance, R_r the rust resistance, C_{dl} the double-layer capacitance, R_{ct} the charge-transfer resistance, W the Warburg resistance or barrier diffusion impedance which was associated with the diffusion of corrosive electrolyte into the iron surface through pores in the rust layer that acted as a diffusion barrier. Due to the surface roughness and energy dispersion, a constant phase angle element (CPE) was introduced to describe the C_{dl} and C_r in the fitting circuits [20].

The electrochemical impedance for the circuit of Fig. 13(b) could be expressed by the following equation:

$$Z = R_S + \frac{1}{Y_r(j\omega)^{n_r} + \frac{1}{R_r + 1/[Y_{dl}(j\omega)^{n_{dl}} + 1/(R_{ct} + Z_W)]}} \quad (1)$$

where Y_r and n_r , Y_{dl} and n_{dl} were constants representing the elements C_r and C_{dl} , respectively, Z_W was the Warburg resistance representing as follows [14]:

$$Z_W = A_W \cdot (j\omega)^{-0.5} \quad (2)$$

where A_W was the modulus of Z_W .

The total impedance for the circuit of Fig. 13(a) could be expressed by the following equation:

$$Z = R_S + \frac{1}{Y_{dl}(j\omega)^{n_{dl}} + \frac{1}{R_{ct}}} \quad (3)$$

The equivalent circuits of Figs. 13(a) and (b) were used to fit the Nyquist and Bode plots of rusted and naked iron, respectively. Fitting data was listed in Table 1. Compared with that of the naked iron, R_{ct} of the rusted one was much smaller, which was attributed to the reduction of the rust accelerating the cathodic reaction. The lower R_{ct} value indicated that the corrosion products formed on the archaeological object were less compact, less continuous, and porous [19]. R_r was usually used to evaluate the corrosion resistance of the rust [13]. Therefore, it could be the rust layer had poor barrier behavior and it cannot effectively prevent the corrosion of iron core, which reached an

agreement with the porous structure of the rust layer mentioned above.

Table 1 Fitting data of impedance parameters in equivalent circuits

Samples	R_s ($\Omega \cdot \text{cm}^2$)	Y_{dl} ($\text{mF} \cdot \text{cm}^{-2} \cdot \text{S}^{-n}$)	n_{dl}	R_{ct} ($\Omega \cdot \text{cm}^2$)	R_r ($\Omega \cdot \text{cm}^2$)	Y_r ($\mu\text{F} \cdot \text{cm}^{-2} \cdot \text{S}^{-n}$)	n_r	A_w ($\Omega \cdot \text{cm}^2 \cdot \text{S}^{-0.5}$)
Naked	75.28	1.80	0.74	675.70				
Rusted	42.10	8.32	0.31	17.01	42.65	0.012	0.92	0.41

Mechanism of the rust growth

The rust growth and iron corrosion mechanism of this archaeological iron could be proposed from the iron surface to the outer rust layer. Since the rust growth of archaeological iron was not an independent process of a single rust phase, it was better to describe the rust growth according to environmental changes in multiple periods.

When the Nanhai I ship was hit by a shipwreck, the cargo on the ship sank into the sea. The iron products began to immerse in a salt-rich water environment and started corroding. The corrosion reactions in initial stage could occur as follows [21].

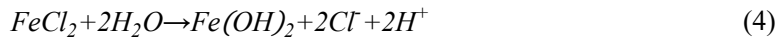
The iron objects worked as an anode region:



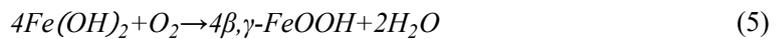
As the ship sinks, a large amount of air would be brought in instantly and attached to the surface of the cargo in the form of bubbles. Hence, the interface between iron and sea water would be a cathodic reduction due to the oxygen dissolved in the thin water film. Meanwhile, countless electrochemical cells involving cathodic and anodic areas were started and scattered on the iron surface to form numerous corrosion sites:



Then, the interface would quickly turn into normal seawater with high chloride concentration, with the consumption and bursting of tiny bubbles. The chloride ions were more readily adsorbed than oxygen in competition for surface sites and deposited on the metal with high retention promoted the formation of ferrous chloride accelerating the corrosion of iron. Besides, the accompanying hydrolysis started to create a weakly acidic environment around it [22]:

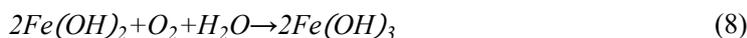


Mud and sand would gradually envelop and cover the archaeological objects with the water flow. Blocking the update and circulation of dissolved oxygen and reserving the chloride ions around the iron. The high chloride concentration and local acidic conditions at the interface gave chances to the formation of FeOOH, especially akaganeite and lepidocrocite [11]:

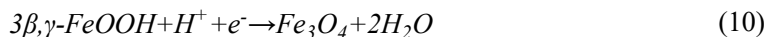


Meanwhile, there some ferrous ions were not chosen to be compounds with chloride ions but forming hydrated ions in solution or oxidized to Fe(OH)₃ which had very low solubility. The intermediate corrosion products FeOH⁺ and Fe(OH)₃ could be converted into γ -FeOOH and δ -

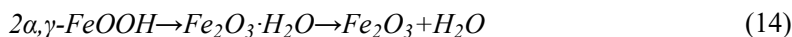
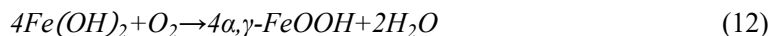
FeOOH with the small amount of oxygen remaining in the mud and sand [21]:



Eventually, the archaeological iron was wrapped and buried tightly under the silt in deep sea, forming an anaerobic and weakly acidic environment. Fe₃O₄ could be reduced and converted rapidly from γ -FeOOH and β -FeOOH [23, 24]. Ferrous ions and electrons could pass through an Fe₃O₄ layer due to its good conductivity. Besides, Fe₃O₄ was prone to accumulate at the interface and form dense layer on the surface of iron under the cathodic reaction [25]. The reduction of the γ -FeOOH and β -FeOOH layer would continue to transform into the cathode area of Fe₃O₄ layer. Meanwhile, the chloride ions would gradually cause local break of the oxide/oxyhydroxide film on the iron objects, especially at rough and uneven surface [26], so the corrosion process of the archaeological iron was slow but unstoppable in the marine for more than 800 years:



After being excavated out of seawater, the archaeological iron was immersed in a weakly alkaline solution and transported to the laboratory for research. For preservation and display, this iron object was placed at room temperature to gradually remove internal moisture. Since the oxygen concentration and humidity changed significantly on the rust surface during drying stage, it was prone to form γ -FeOOH again and α -FeOOH. At this stage, γ -FeOOH and α -FeOOH could be generated by oxidizing the precipitation of Fe(OH)₂ derived from the outer rust, and only a fraction of FeOOH was generally adsorbed on the surface of outermost layer. The structure of newly generated FeOOH was loose and did not cover the objects tightly resulting in the formation of pores in yellow rust. Hence, when the archaeological iron was removed from dechlorination solution or rinsed with distilled water, it was easily detached. After the immersing in alkaline solution, FeOOH in the dehydration stage was more likely to form maghemite and hematite [18]:



Conclusions

Archaeological iron artifacts excavated from the Nanhai I ancient ship were corroded and fragmented on a large scale. The metallographic structure of them belonged to hypereutectic white cast iron with carbon content of 4.3-6.69 wt.% and experienced low melt undercooling. There were many cracks in the iron core caused by general corrosion, which was the direct cause of the fragmentation.

Further, the upper rust of the archaeological iron was most corroded which could be distinguished in two layers. The outer layer was loose yellow rust, mainly composed of α -Fe₂O₃, γ -Fe₂O₃, α -FeOOH, γ -FeOOH, and δ -FeOOH. The dense black rust layer close to the iron core was gathered β -FeOOH and Fe₃O₄ with full of threatening chlorine which could break this dense layer. Meanwhile, there were also many cracks in the rust layers extending to the iron surface which resulting in a very low resistance against the seawater indicated that the rust was a poor barrier of the internal metal. Both were the important reasons for general corrosion of the archaeological iron.

There was a reasonable mechanism proposed to explain the growth and transformation of each rust layer and the reason why the rust layer cracked and lost its protective effect, which combined corrosion conditions and reactions from the initial stage being submerged in seawater to the state before laboratory protection.

For the better conservation of these archaeological irons, the rust should be rigorously dechlorinated and stabilized with proper corrosion inhibition and reinforcement. Moreover, the preservation status should be monitored in daily routine.

Acknowledgements

Thanks to Ms. Li Chen in School of Physics, Peking University, for her support of SEM and EDS in this work.

Authors' contributions

Minghao Jia performed the research and wrote the manuscript.

Pei Hu, Zisang Gong, Yadong Xue, and Yufan Hou analyzed the data together.

Gang Hu, Dongbo Hu, Jian Sun, and Yong Cui edit the manuscript and provide academic guidance.

All authors read and approved the final manuscript.

Funding

This work was supported by the National Key Research and Development Program of China (No. 2020YFC1522103).

Availability of data and materials

The data is available within the article.

Declarations**Ethics approval and consent to participate**

Not applicable.

Consent for publication

Written informed consent for publication was obtained from all participants.

Competing interests

The authors declare that they have no competing interests.

Author details

¹School of Archaeology and Museology, Peking University 100871, Beijing, China.

²National Centre for Archaeology, 100013, Beijing, China.

³Guangdong Provincial Institute of Cultural Relics and Archaeology, 510075, Guangzhou, China.

References

1. Hao XL, Zhu TQ, Xu JJ, Wang YR, Zhang XW. Microscopic study on the concretion of ceramics in the "Nanhai I" shipwreck of China, Southern Song Dynasty (1,127-1,279 AD). *Microsc Res Techniq.* 2018;81(5):486-93.
2. Wang Y, Xiao D. The excavation of the "Nanhai No. 1" shipwreck of the Song Dynasty in 2014. *Archaeology.* 2016;12:56-83.
3. Wan X, Mao Z, Zhang Z, Li X. Analysis of iron pans and iron nails unearthed from Nanhai I shipwreck. *Chin Cult Herit Sci Res.* 2016;2:46-51.
4. Remazeilles C, Neff D, Bourdoiseau JA, Sabot R, Jeannin M, Refait P. Role of previously formed corrosion product layers on sulfide-assisted corrosion of iron archaeological artefacts in soil. *Corros Sci.* 2017;129:169-78.
5. Gao XL, Han Y, Fu GQ, Zhu MY, Zhang XZ. Evolution of the rust layers formed on carbon and weathering steels in environment containing chloride ions. *Acta Metall Sin-Engl.* 2016;29(11):1025-36.
6. Kamimura T, Hara S, Miyuki H, Yamashita M, Uchida H. Composition and protective ability of rust layer formed on weathering steel exposed to various environments. *Corros Sci.* 2006;48(9):2799-812.
7. Saleh SA. Corrosion mechanism of iron objects in marine environment an analytical investigation study by Raman spectrometry. *Eur J Sci Theol.* 2017;13(5):185-206.
8. Bazan AM, Galvez JC, Reyes E, Gale-Lamuela D. Study of the rust penetration and circumferential stresses in reinforced concrete at early stages of an accelerated corrosion test by means of combined SEM, EDS and strain gauges. *Constr Build Mater.* 2018;184:655-67.
9. Mazur A, Gasik MM, Mazur VI. Thermal analysis of eutectic reactions of white cast irons. *Scand J Metall.* 2005;34(4):245-9.
10. Veneranda M, Aramendia J, Bellot-Gurlet L, Colombari P, Castro K, Madariaga JM. FTIR spectroscopic semi-quantification of iron phases: A new method to evaluate the protection ability index (PAI) of archaeological artefacts corrosion systems. *Corros Sci.* 2018;133:68-77.
11. Liu YW, Wang ZY, Wei YH. Influence of seawater on the carbon steel initial corrosion behavior. *Int J Electrochem Sci.* 2019;14(2):1147-62.
12. Labbe JP, Ledion J, Hui F. Infrared spectrometry for solid phase analysis: Corrosion rusts. *Corros Sci.* 2008;50(5):1228-34.
13. Nishimura T, Katayama H, Noda K, Kodama T. Electrochemical behavior of rust formed on carbon steel in a wet/dry environment containing chloride ions. *Corrosion.* 2000;56(9):935-41.
14. Li QX, Wang ZY, Han W, Han EH. Characterization of the rust formed on weathering steel exposed to Qinghai salt lake atmosphere. *Corros Sci.* 2008;50(2):365-71.
15. Rocca E, Faiz H, Dillmann P, Neff D, Mirambet F. Electrochemical behavior of thick rust layers on steel artefact: Mechanism of corrosion inhibition. *Electrochim Acta.* 2019;316:219-27.
16. Ouyang W. μ Raman Analysis of the Rust Layer on Rusted Cast Iron Artifacts. *Adv Mater Res.* 2014;887-888:262-5.
17. Bernard MC, Joiret S. Understanding corrosion of ancient metals for the conservation of cultural heritage. *Electrochim Acta.* 2009;54(22):5199-205.
18. Calero J, Alcantara J, Chico B, Diaz I, Simancas J, de la Fuente D, et al. Wet/dry accelerated laboratory test to simulate the formation of multilayered rust on carbon steel in marine atmospheres. *Corros Eng Sci Techn.* 2017;52(3):178-87.
19. Dhaiveegan P, Elangovan N, Nishimura T, Rajendran N. Electrochemical characterization of carbon and weathering steels corrosion products to determine the protective ability using carbon paste

- electrode (CPE). *Electroanal.* 2014;26(11):2419-28.
20. Han D, Jiang RJ, Cheng YF. Mechanism of electrochemical corrosion of carbon steel under deoxygenated water drop and sand deposit. *Electrochim Acta.* 2013;114:403-8.
 21. Hu JY, Cao SA, Xie JL. EIS study on the corrosion behavior of rusted carbon steel in 3% NaCl solution. *Anti-Corros Method M.* 2013;60(2):100-5.
 22. Zheng LG, Yang HY. Influence of organic inhibitors on the corrosion behavior of steel rebar inside mortar specimens immersed in saturated NaCl solution. *Acta Phys-Chim Sin.* 2010;26(9):2354-60.
 23. Ishikawa T, Kondo Y, Yasukawa A, Kandori K. Formation of magnetite in the presence of ferric oxyhydroxides. *Corros Sci.* 1998;40(7):1239-51.
 24. Tanaka H, Mishima R, Hatanaka N, Ishikawa T, Nakayama T. Formation of magnetite rust particles by reacting iron powder with artificial α -, β - and γ -FeOOH in aqueous media. *Corros Sci.* 2014;78:384-7.
 25. Evans UR. Electrochemical mechanism of atmospheric rusting. *Nature.* 1965;206(4988):980-2.
 26. Allam IM, Arlow JS, Saricimen H. Initial stages of atmospheric corrosion of steel in the arabian gulf. *Corros Sci.* 1991;32(4):417-32.

Figures



Figure 1

Archaeological iron artifacts coming from Nanhai I (Guangdong, China) with rust

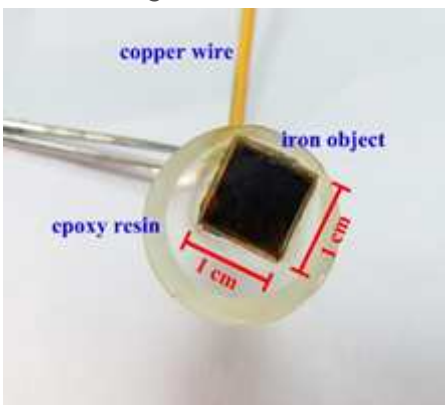


Figure 2

Working electrode for electrochemical impedance test

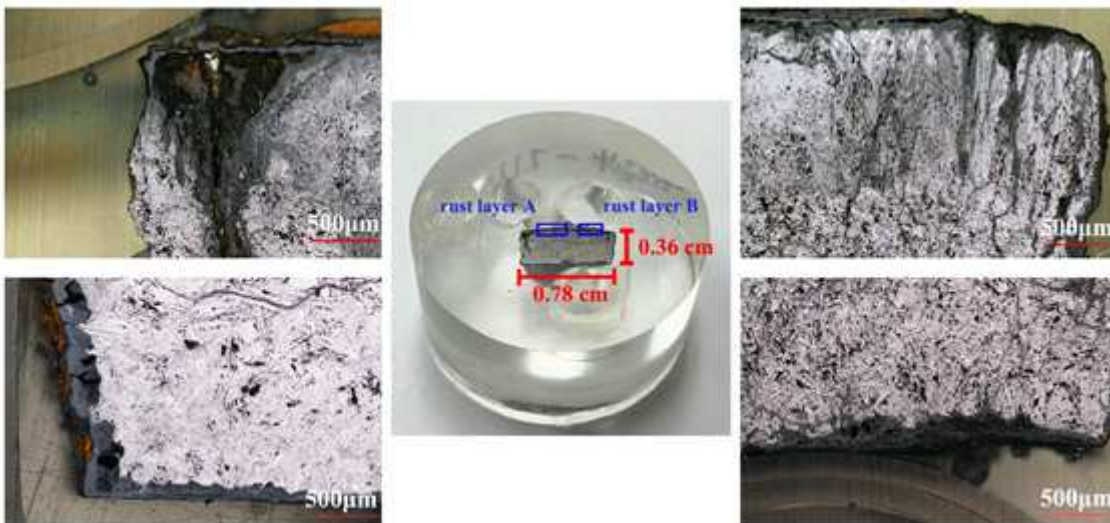


Figure 3

Digital and microscopic graphs of the cross-section of archaeological iron

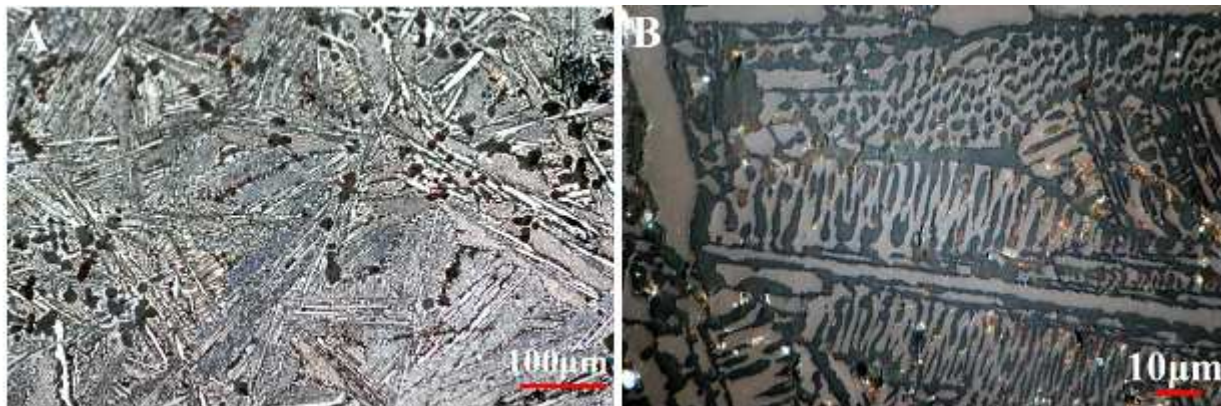


Figure 4

Metallographic diagrams of archaeological iron artifact from Nanhai I

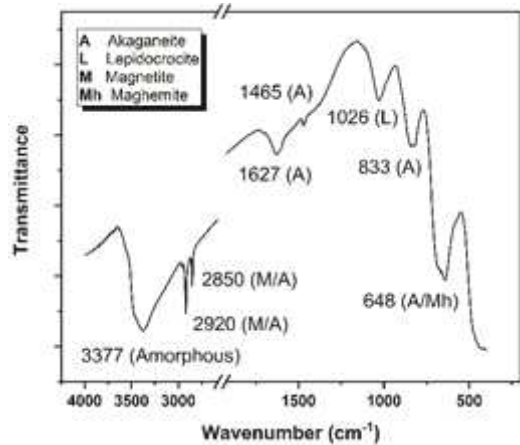


Figure 5

FT-IR diagram of rust powder

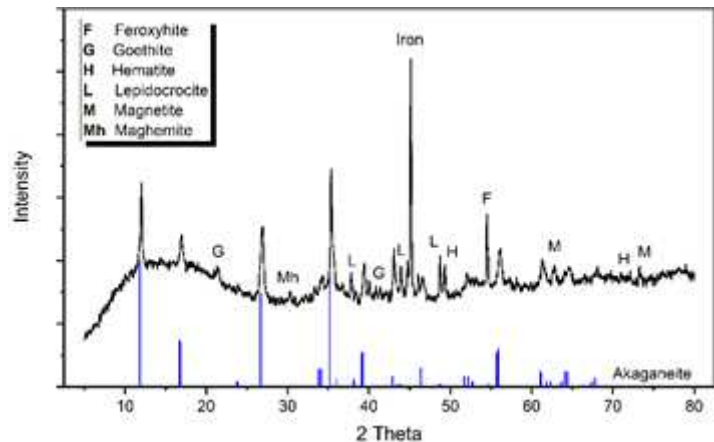


Figure 6

XRD diagram of rust powder

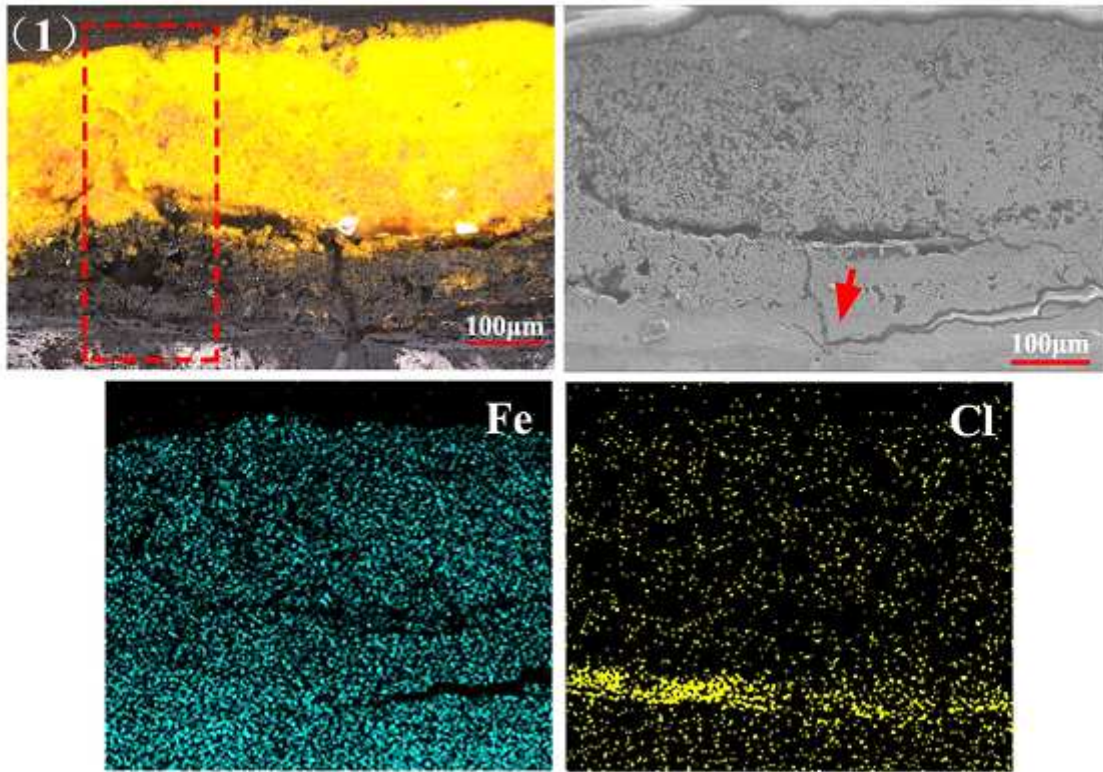


Figure 7

Graphs of microstructure and element distribution of the rust layer A (red square for Raman analysis)

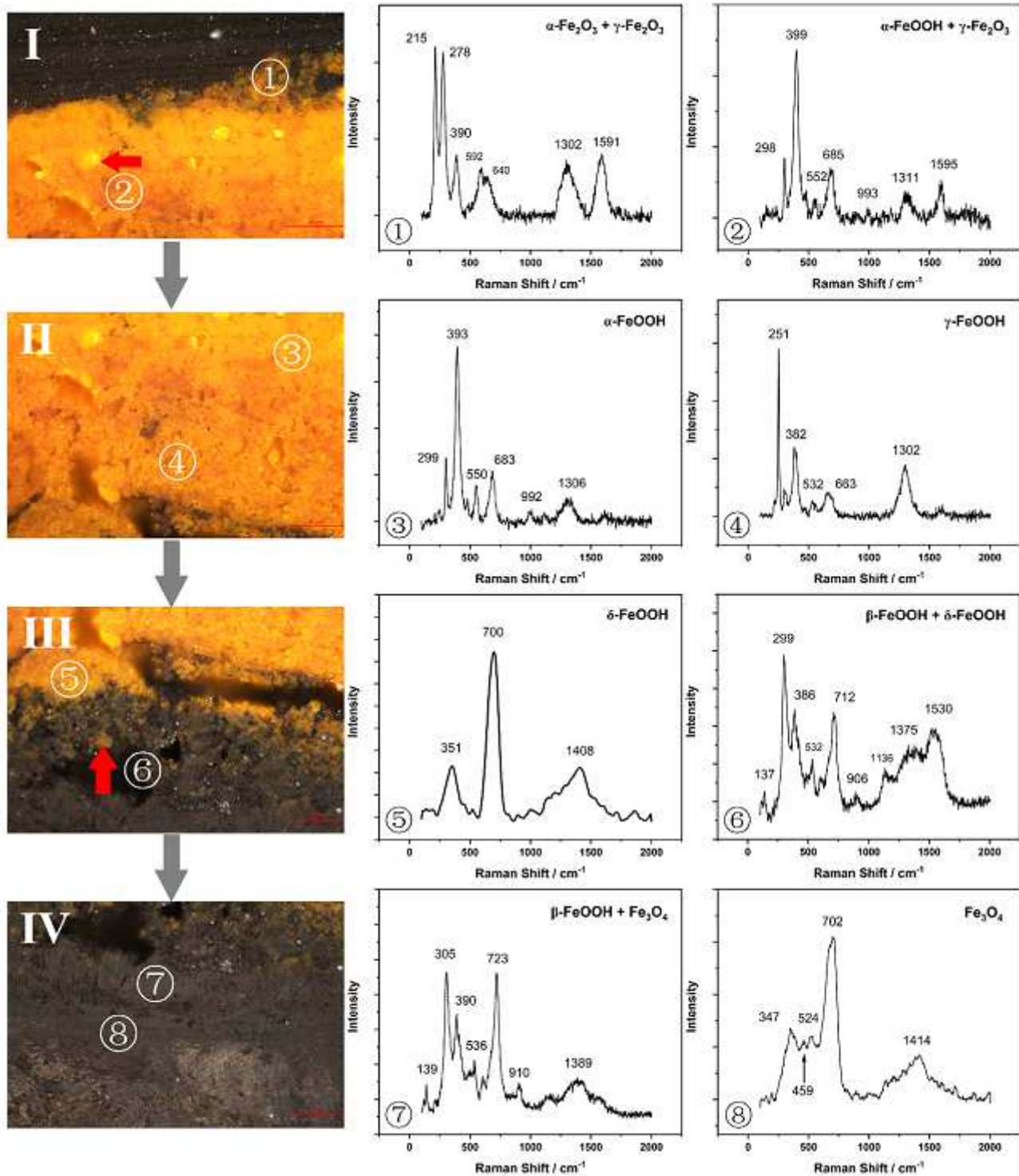


Figure 8

Raman spectra of the rust layer A (red square in Fig. 7)

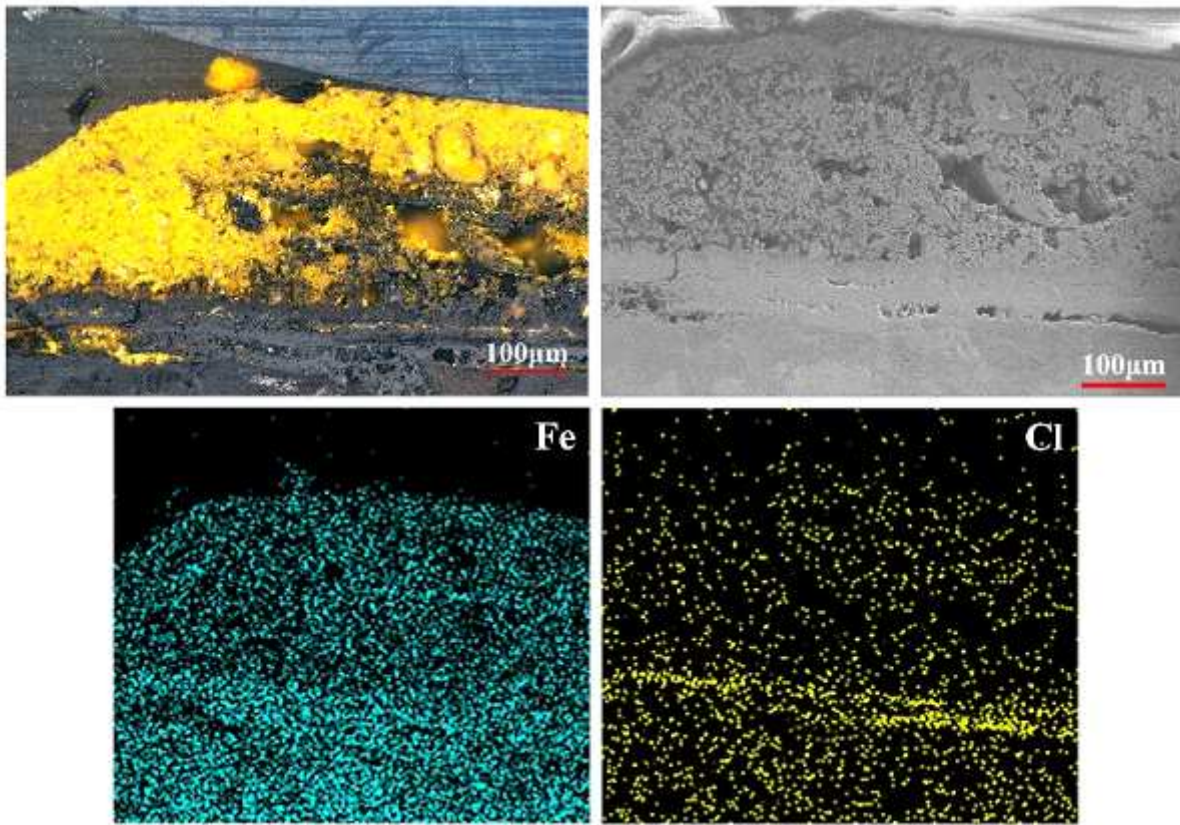


Figure 9

Graphs of microstructure and element distribution of the rust layer B

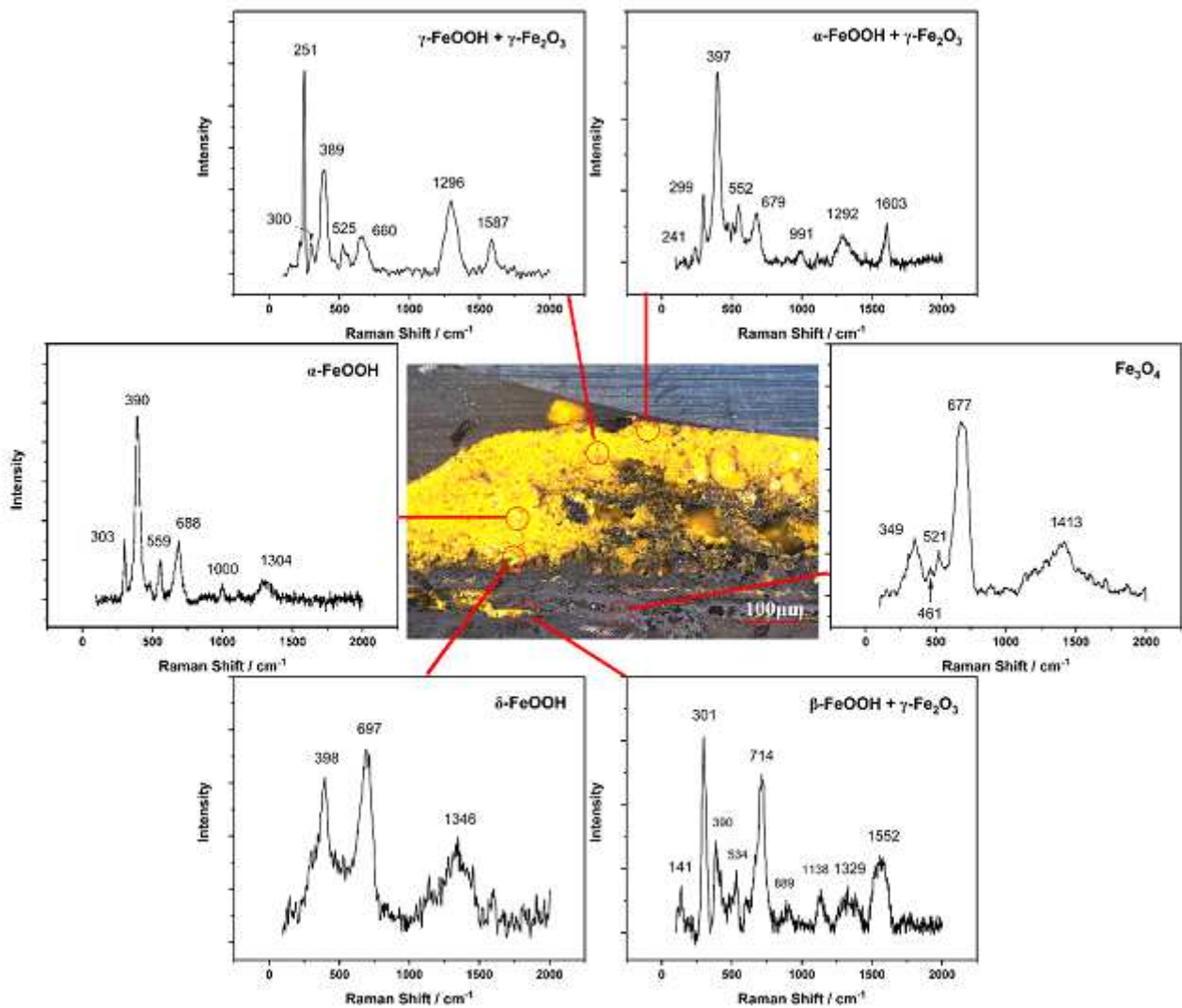


Figure 10

Raman spectra of the rust layer B

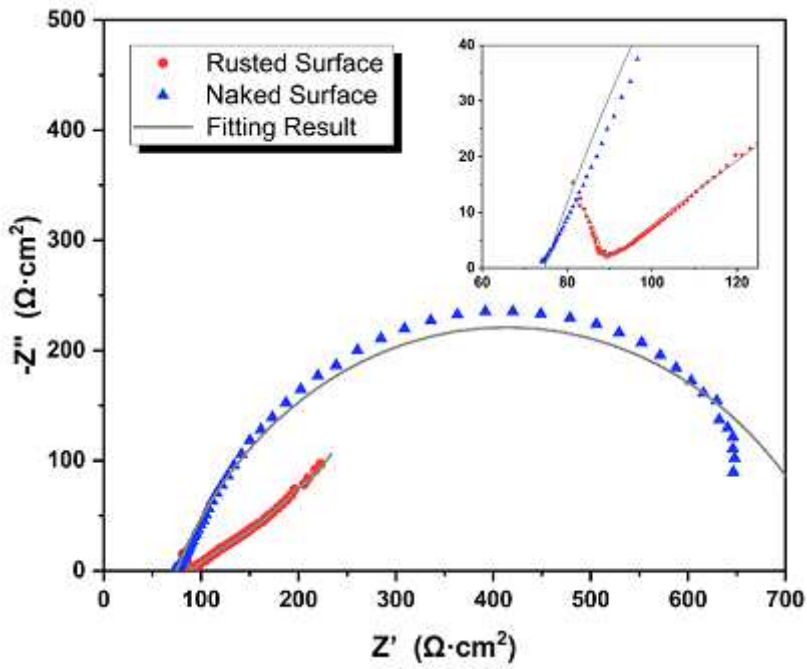


Figure 11

Nyquist plots of naked and rusted archaeological iron in simulated seawater

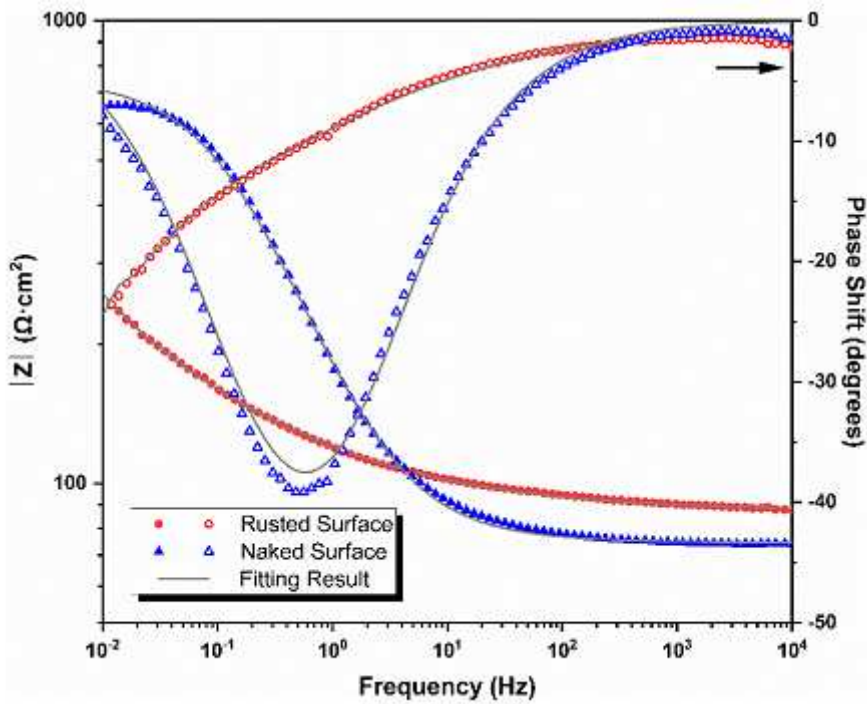


Figure 12

Bode plots of naked and rusted archaeological iron in simulated seawater

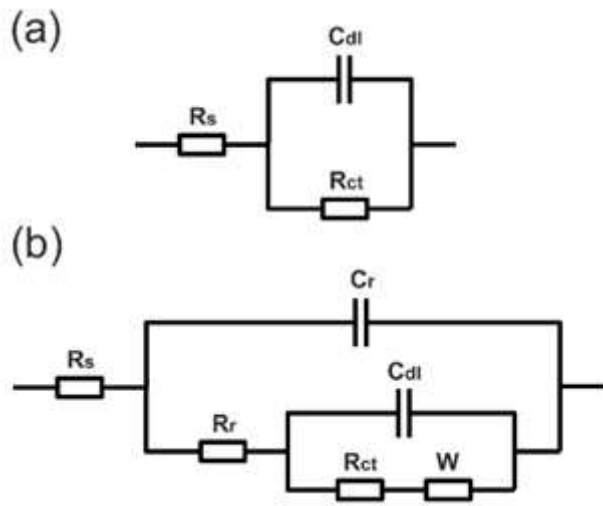


Figure 13

Equivalent circuit of naked and rusted archaeological iron